OPEN ACCESS

University of BRISTOL

Ali, A., De Risi, R., & Sextos, A. (2021). Seismic assessment of wind turbines: How crucial is rotor-nacelle-assembly numerical modeling? *Soil Dynamics and Earthquake Engineering*, *141*, [106483]. https://doi.org/10.1016/j.soildyn.2020.106483

Peer reviewed version

License (if available):
CC BY-NC-ND

Link to published version (if available):
10.1016/j.soildyn.2020.106483

Link to publication record in Explore Bristol Research
PDF-document

This is the author accepted manuscript (AAM). The final published version (version of record) is available online via Elsevier at https://www.sciencedirect.com/science/article/pii/S026772612031109X . Please refer to any applicable terms of use of the publisher.

University of Bristol - Explore Bristol Research
General rights

This document is made available in accordance with publisher policies. Please cite only the published version using the reference above. Full terms of use are available:
http://www.bristol.ac.uk/red/research-policy/pure/user-guides/ebr-terms/

Seismic assessment of wind turbines: how crucial is rotor-nacelle-assembly numerical modeling?

Ahmer Ali, Raffaele De Risi, Anastasios Sextos

Department of Civil Engineering, University of Bristol, United Kingdom

Abstract

The cross-section and the structural twist angle of a typical wind turbine blade vary along its span. This complicates its realistic modeling in nonlinear dynamic analysis of wind turbines when seismic performance estimates are sought. As a result, the lumped mass approach is most commonly used to model the rotor-nacelle-assembly (RNA). The RNA is eccentric to the tower top, and the blades tend to induce rotary inertia on the tower. The exclusion of this rotary inertia and the rotor eccentricity can impact the structural response of the wind turbines as the RNA contributes significantly to the total mass of the system. Moreover, the blades are long, slender structural components that can vibrate and deform independently under seismic excitation. The lumped mass approach intrinsically considers the rigid-body inertia for the RNA, which inevitably acts as a part of the tower top. This can affect the seismic vulnerability estimation of the offshore wind turbines (OWT) at a degree that has not yet been properly quantified. To explore this issue, the present study discusses the effects of the three key RNA parameters, i.e., (i) rotary inertia of the blades, (ii) rotor eccentricity, and (iii) blades' flexibility, on the seismic failure and fragility of OWT under shallow crustal earthquakes. Results show that the rotary inertia affects the higher modes, which in turn influence the height of the tower failure zones. It is also shown that different levels of RNA modeling refinement affect the predicted failure probabilities, particularly under pulse-like ground motions, while the same estimates are overestimated if the conventional rigid body lumped mass rotary inertia is used. Even worse, they can be underestimated (thus less safe) when the rotary inertia is completely ignored, compared with the refined modeling of flexible turbine blades. These results are revealing as they highlight that seismic hazard can indeed pose a significant design issue for OWTs in some regions.

Keywords

Renewable energy; Offshore wind turbines; Blade deformability; Tower failure zones; Seismic vulnerability

1. Introduction

The development of a reliable computational model is of paramount importance for structural analysis in a probabilistic seismic risk assessment (PSRA) framework. The complexity of the numerical model depends on the required structural response and the desired computational efficiency. The modeling approach can vary from a simple one-dimensional (1D) beam element model [1,2] to a complex 3D finite element model (FEM) [3,4]. One-dimensional beam element models are suitable for simulating the global structural response [5]. At the same time,

a detailed 3D FEM is efficient for investigating the local yielding/instabilities in structural components [6–8], e.g. plastic hinges, buckling ovalisation effects, etc. Similarly, 1D FEMs are developed to study various soil-structure interaction problems, where details for considering soil nonlinearity, soil impedance, as well as kinematic interaction are often approximated through simplified material laws, springs, and dashpots, respectively [9–12]. For more insightful quantification on wave propagation effects, soil fatigue, discontinuity at the soil-pile interface, advanced nonlinear 3D soil models with detailed material constitutive laws are often preferred [13–20]. Independently of the modeling approach, each computational model must be defined in terms of structural parameters such as mass, stiffness, damping, strength, boundary conditions, etc. The reliability of the structural response depends on how rigorously the uncertainties in these parameters are considered [21]. The ground motion variability (i.e. the aleatory uncertainty component) is usually deemed more significant to affect the structural response [22], therefore, structural parameters are often treated in a simplified manner to reduce the computational effort.

The rotor-nacelle-assembly (RNA) is a combination of essential structural components, i.e. nacelle, gearbox, and rotor (i.e., hub and blades combined) that transform wind energy to electrical power. The general details on an RNA, such as the rotor diameter, nacelle, hub, and the blades' mass are easily available [2,23,24] and as such, quite simple to model. The local details of the blades, however, including their shape profile, material distribution, and strength are often difficult to find because the aerodynamic profile of the blades is patented and represents an offshore industry asset. As a result, it is a common practice to simplify the RNA atop the tower as a point mass [2,5–8,25]. This is a robust and time-efficient choice for the RNA modeling, particularly when a nonlinear numerical analysis is performed and an extensive set of earthquake ground motions are used [2,6,25]. Notwithstanding the above advantages, the lumped mass approach makes a major simplification: it considers the RNA as a rigid body, ignoring the effects of the blade deformability as well as that of local blade modes and their modal damping on the global structural response of the turbine.

In a typical RNA, nacelle and rotor are generally eccentric to the tower, both horizontally and vertically. The nacelle dominates the total RNA mass (M_{RNA}) which can be up to half of the total wind turbine's mass [23], and it is shown to be one of the driving parameters to identify the nature and location of tower failure in offshore wind turbines (OWT) under crustal earthquakes [5]. Besides, blades are long, slender structures that tend to induce rotary inertia effects at the tower due to their ability to vibrate individually. Such an effect can be generically considered into a numerical analysis if the full blades are modeled [3]. However, it has to be invoked through analytical computations into a structural model, if a lumped mass is used [2]. In this regard, there is a variety of modeling methods to capture the three main RNA parameters, i.e., (i) rotary inertia of the blades, (ii) the rotor/RNA eccentricity, and (iii) the deformability of the blades. Ideally, the first and the third parameter represent the same quantity, i.e., the rotary inertia of the blades. However, in this study, the first parameter is assumed to relate to the lumped mass approach, whereas the third parameter corresponds to the explicit modeling of the blades. This conceptual distinction aims to serve the comparative study of their effect on the prediction of seismic performance at a structural (i.e. OWT) level. Depending on the modeling approach, both these parameters can be considered in conjunction with the second parameter. There has been a limited number of studies that consider the rotary inertia and the rotor eccentricity simultaneously, where the latter is taken as either only vertical [2,5] or in both horizontal and vertical directions [3,7,8,26]. But, so far, it is unclear how the

interaction of these RNA parameters impacts the structural behavior and vulnerability of wind turbines under seismic actions.

1.1. Novelty and scope of this work

This study aims at evaluating the effects of rotary inertia of the blades and the rotor eccentricity on the nonlinear structural response and failure probabilities of OWTs. The rotor inertia of the blades is considered using the conventional lumped mass approach and the explicit modeling of the full blades. This is done to further examine the influence of blades' deformability and their local modes on the failure and seismic fragility of OWT towers. An important point here is that OWTs are shown to be vulnerable to crustal earthquakes [2,5]. Therefore, a bin (subset) of 100 shallow crustal earthquake records is selected for nonlinear dynamic analysis, split into 50 pulse-like and 50 non-pulse-like records. The changes in the tower failure modes, their location, and their failure probabilities [27] are examined using five different combinations of the rotary inertia and the rotor eccentricity. First, the rotary inertia of the blades (I_R) is ignored and the M_{RNA} is assigned to the tower top. Second, the I_R is also applied at the tower top, which is computed assuming a uniform distribution of the blade mass (m_B) across the blade length (r_B). Third, a vertical eccentricity of M_{RNA} and I_R above the tower top is considered. Fourth, the nacelle (m_N) and the rotor mass (m_R) are considered with a vertical and a horizontal eccentricity from the tower top. m_N and m_R are placed at their center of mass locations, whereas the I_R is applied at m_R. Fifth, the blades are modeled explicitly where the rotary inertia is induced using their cross-section properties. The modal, nonlinear dynamic, and fragility analysis results are then discussed to point out the implications of the different pairs of RNA parameters on the high-order vibration modes, tower failure modes, their location, and the failure probabilities predicted for OWTs under pulse-like and non-pulse-like crustal earthquakes.

2. Structural model

The structural specifications of the NREL 5MW reference offshore wind turbine (OWT) [23], supported on a monopile foundation [28], are considered. The numerical model of the 5MW OWT is developed using the OpenSees software [29]. Figure 1 shows the schematic description of the OWT geometry, the global axis, and the finite element model (FEM). The main tower, transition piece, and the monopile are modeled using nonlinear beam-column elements. It is a robust and time-efficient choice for the supporting tower, especially when an extensive bin of earthquake time histories are involved to analyze the global system behavior, including buckling [2,5]. The Batdorf curvature parameter for thin cylindrical shells is used for element discretization [30]. The main tower, transition piece, and the monopile have an element length of 0.7 m, 0.9 m, and 1.2 m, respectively. This size assures that the elements act as intermediate shells where the section's strength is mobilized in the event of global tower buckling [5]. It is noted that the effects of bolts, welds, and flanges are not considered in the tower. Therefore, an increased steel density of 8500 kg/m^3 is used, following recommendations from the literature [23]. Moreover, the presence of the doorway and production imperfections are excluded, which may slightly underestimate the structural response [7].

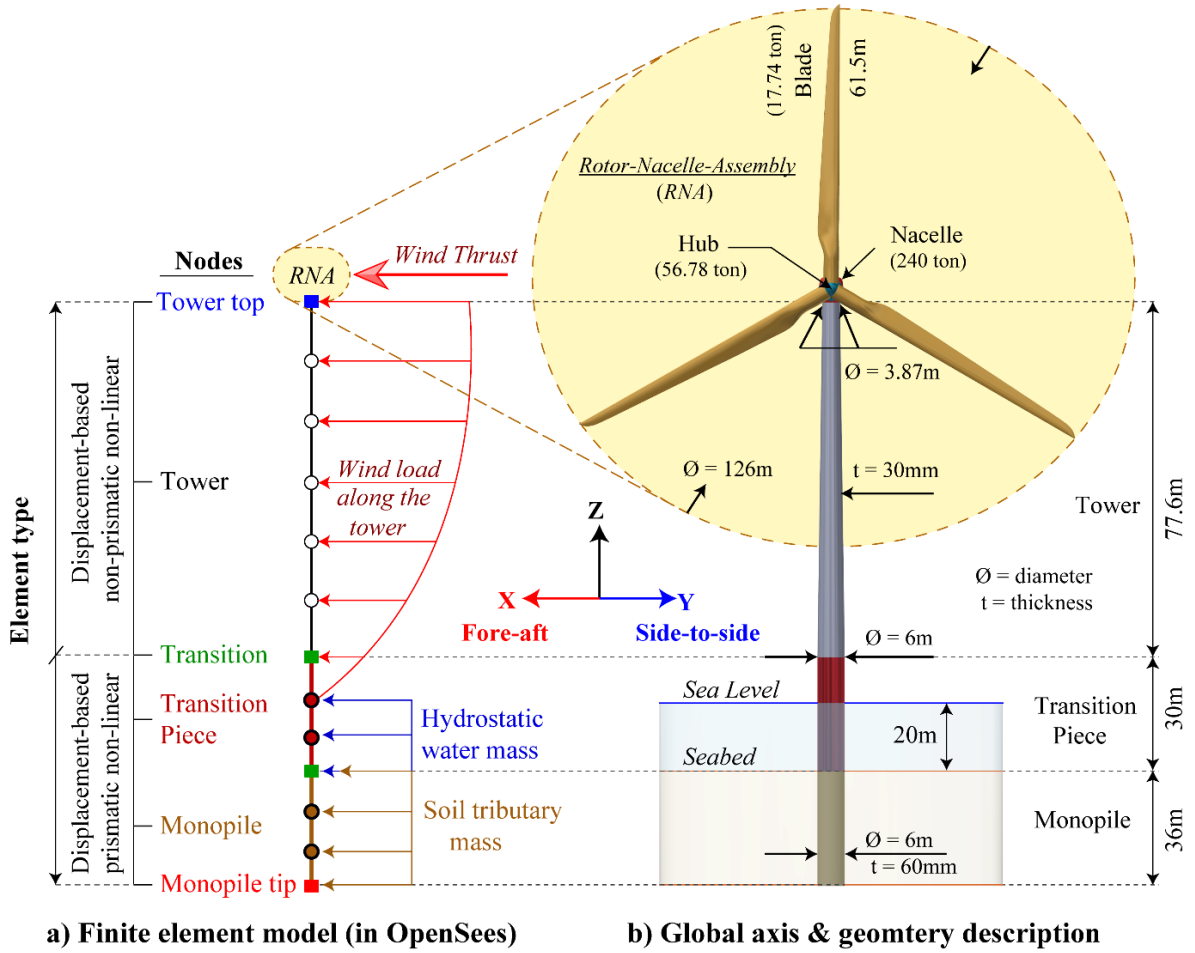

a) Finite element model (in OpenSees) **b) Global axis & geomtery description**

Figure 1 Schematic representation of the OWT (a) Finite element model; (b) geometry, and reference global axis

The soil-monopile interaction is modeled as a beam on nonlinear springs to represent the mechanical behavior of the soil around the monopile[1]. The input geotechnical properties include soil's unit weight (10 kN/m^3), internal friction angle (35°), and soil shear modulus (250 MPa) at the pile tip [5,28]. Figure 2(a-c) explains the modeling schematics of the soil springs, generated using zero-length elements. Each spring element includes two nodes where one is fully constrained (fixed node), while the other (slave node) is connected to the monopile (master node) having an equal degree of freedom, i.e. free translations and constrained rotations [2]. Soil resistance is modeled in the horizontal and vertical directions through independent uniaxial materials. *p-y* springs through *PySimple*1 [10] material object in OpenSees [29], where the ultimate load curves and subgrade reaction coefficient along the monopile depth follow the recommendations of the American Petroleum Institute (API) [31]. Similarly, the vertical soil resistance along the monopile is modeled through *TzSimple*1 material by means of a *t-z* backbone relation for axially loaded piles in the sand as proposed by Mosher [32]. *Q-z* spring is another vertically-oriented spring to model the soil behavior at the monopile tip using *QzSimple*1 material with *q-z* relation for compression versus uplift given by Vijayvergiya [33].

[1] https://opensees.berkeley.edu/wiki/index.php/Laterally-Loaded_Pile_Foundation

Figure 2(d-f) shows the hysteretic behavior of *PySimple*1[2], *TzSimple*1[3], and *QzSimple*1[4] material under cyclic loading. It is possible to consider the gapping effects on the monopile [10,11], and use dashpots coupled with nonlinear soil springs to emulate radiation damping [9,10,12]. However, such details are neglected in this study due to the limited available geotechnical details. Advanced nonlinear models are required for better quantification of discontinuity at the soil-pile interface, seismic wave propagation, and energy dissipation [14–19,34–37], however, this remains out of the present scope.

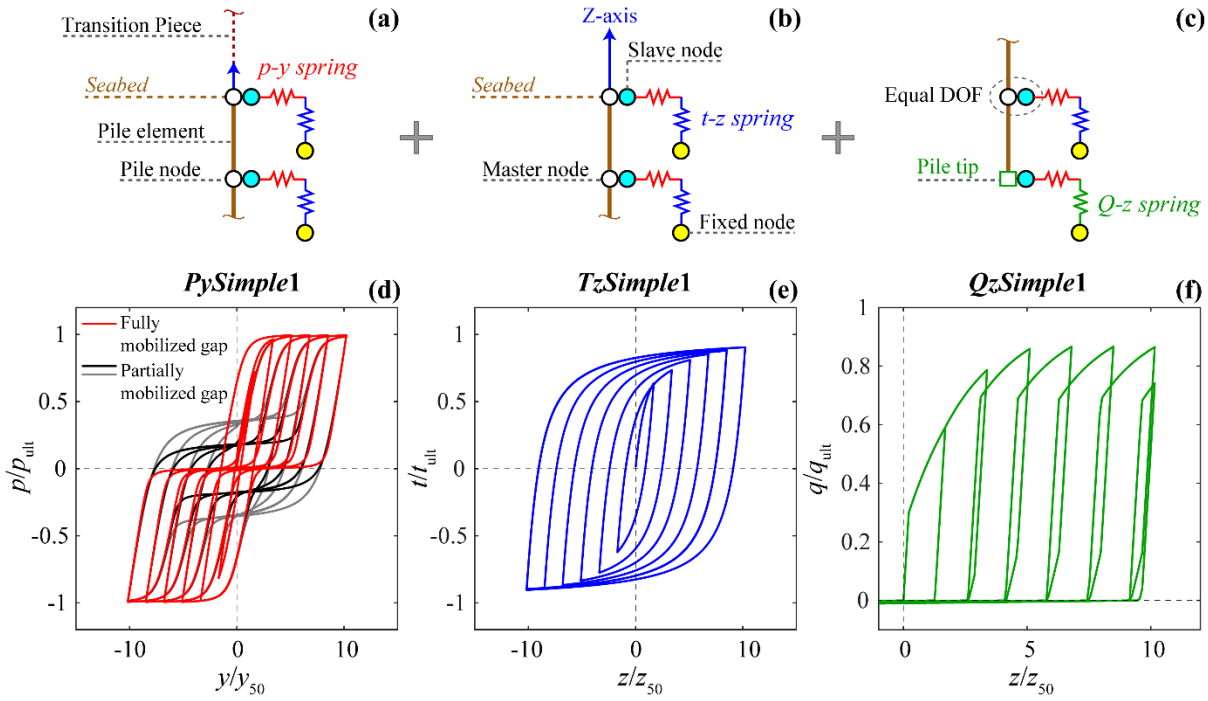

Figure 2 Modeling schematics and material hysteretic behavior of nonlinear soil springs; (a, d) horizontal *p-y* spring with *PySimple*1 material [10,31]; (b, e) vertical *t-z* spring with *TzSimple*1 material [32]; (c, f) pile tip *Q-z* spring with *QzSimple*1 material [33].

2.1. Load modeling

Apart from the self-weight, four types of loadings are considered in this study, i.e., the wind load, the effect of water mass around the monopile, the effect of the tributary soil mass surrounding and inside the monopile, and the seismic loads. All the loads are modeled statically, except the earthquake loads which are modeled in a dynamic regime for nonlinear response history analysis.

All structural and non-structural masses, including the main tower, transition piece, monopile, rotor-nacelle-assembly (RNA), hydrostatic water, and the soil, are applied at the structural nodes as shown in Figure 1. The water mass is calculated as 80% of the transition piece mass under the sea level. The tributary area to compute the soil mass inside and around the monopile is considered equivalent to the monopile area [2,5]. The wind load is considered as the concentrated nodal loads, applied along the supporting tower above the sea level, following the

[2] https://opensees.berkeley.edu/wiki/index.php/PySimple1_Material
[3] https://opensees.berkeley.edu/wiki/index.php/TzSimple1_Material
[4] https://opensees.berkeley.edu/wiki/index.php/QzSimple1_Material

normal wind profile from the ASCE/SEI [38] and IEC [39] regulations, for a reference wind speed of 15 m/s. Also, a thrust force arising from the influence of the wind on the blades is applied at the rotor hub; refer to [40,41] for details on its evaluation procedure.

The earthquake loads are applied in all three directions, i.e., two horizontal (X, Y) and one vertical (Z), using acceleration time histories. To maximize the loading effects, the stronger of the two horizontal ground motions, in terms of the peak ground acceleration (PGA), is applied in the direction of the wind load, i.e., fore-aft (X) direction. The load combination factors, of course, should be appropriately quantified in a design situation, however, this is not deemed necessary herein given that the focus is on the relative effect of different degrees of FE modeling refinement. Ground motions are applied uniformly along the pile length (i.e., at the pile spring supports). This is a simplification given that the frequency and amplitude of seismic waves tend to alter while propagating through the soil media [19]. Vertical propagation of S-waves may induce additional bending moments through soil-pile kinematic interaction [42–44]. Given the lack of stratigraphic geotechnical details, it is neither possible to perform a site response and wave propagation analysis nor to develop a free-field soil column connected to soil springs, therefore, excitations are deemed uniform along the pile length. It should be noted that this may lead to a slight underestimation of the response in OWTs, especially for the case of layered [45] or liquefiable soils [46].

2.2. Rotor Inertia Modeling

This study uses five different RNA configurations for the OWT numerical model. These configurations are selected to capture the influence of the blades' rotary inertia and rotor eccentricity on the dynamic behavior and seismic fragilities of OWTs. Figure 3 shows the schematics of a typical RNA and sketches the five rotor-inertia modeling configurations, studied here. These configurations are termed as C1 to C5, where the first-four uses the lumped mass approach with different assumptions and the last considers the full three-blades to model the rotary inertia. More specifically, C1 considers the total RNA mass (M_{RNA}) at the tower top, while ignoring the rotor eccentricity and inertia (I_R) (Figure 3c). C2 extends C1 by considering I_R, such that I_R is transferred to the M_{RNA} node by an amount of ex_R, which is the horizontal distance between the hub and the tower (Figure 3d). C3 further introduces the vertical eccentricity (ez_S) of M_{RNA}, where ez_S is the location of the rotor shaft above the tower top (Figure 3e). C4 disintegrates the RNA mass, such that the nacelle mass (m_N) is separately placed at a horizontal (ex_N) and a vertical distance (ez_N) away from the tower top. Similarly, the rotor mass (m_R) is eccentric to the tower by an amount ex_R and ez_R. In this case, m_R is the combined mass of the hub (m_H) and three blades ($3\times m_B$), where the I_R is directly applied at the m_R node (Figure 3f).

The I_R for C1 to C4 is calculated using equations (1) to (3), assuming uniform mass distribution along the length (r_B) of each blade [2]. I_X, I_Y, and I_Z refer to the moment of inertia about the global X, Y, and Z-axis, respectively. C5 is an extension to C4, and it refers to a blade-integrated configuration, as shown in Figure 3g. The hub and blades are modeled separately. Thus, the contribution of I_R comes from the cross-sectional stiffnesses of the blade $(I_B)_{i\,=\,1,\,\ldots,\,n}$, where n is the total number of the blade's cross-sections. Equation (4) is used to estimate the torsional ($I_x = J$), flapwise (I_y), and edgewise (I_z) moments of inertia of an *ith* section of the blade about its local x, y, and z-axis, respectively [47]. A refers to the area of a hollow thin-

walled blade section (airfoil), *t* is its wall thickness, *l* is its perimeter length, *c* is its chord length or the width, and *dA* is its differential area.

C1: $$I_{\mathrm{R}} = \{I_{\mathrm{X}} = I_{\mathrm{Y}} = I_{\mathrm{Z}} = 0 \quad (1)$$

C2, C3: $$I_{\mathrm{R}} = \begin{cases} I_{\mathrm{X}} = m_{\mathrm{B}} r_{\mathrm{B}}^2 \\ I_{\mathrm{Y}} = I_{\mathrm{Z}} = 0.5 m_{\mathrm{B}} r_{\mathrm{B}}^2 + 3 m_{\mathrm{B}} e x_{\mathrm{R}}^2 \end{cases} \quad (2)$$

C4: $$I_{\mathrm{R}} = \begin{cases} I_{\mathrm{X}} = m_{\mathrm{B}} r_{\mathrm{B}}^2 \\ I_{\mathrm{Y}} = I_{\mathrm{Z}} = 0.5 m_{\mathrm{B}} r_{\mathrm{B}}^2 \end{cases} \quad (3)$$

C5: $$(I_{\mathrm{B}})_{i=1,\ldots,n} = \begin{cases} I_{x,i} = J_i = (4 A^2 t/l)_i \\ I_{y,i} = \left(\int_0^c z^2 dA\right)_i \\ I_{z,i} = \left(\int_0^c y^2 dA\right)_i \end{cases} \quad (4)$$

For tower-eccentric RNA configurations, rigid links are used to achieve a rigid kinematic coupling between the RNA nodes. Only one rigid link is used to connect the vertically-eccentric M_{RNA} (master node) to the tower top (slave node), as shown in Figure 3e for C3. However, for a more discrete RNA, i.e., C4, a total of three rigid links are used to connect the rotor shaft node (master) with the tower top nacelle (m_{N}) and rotor (m_{R}) nodes, as shown in Figure 3f. In the case of C5, all three blades are tied to the hub node (m_{H}), and the kinematic coupling among the nacelle, rotor shaft, hub, and the tower top is identical to C4 [48].

2.2.1. Blade FEM and properties

Figure 3g also shows the OpenSees FEM details of a 61.5 m blade used in this study. The blade discretization, cross-sectional shape type and distribution, structural twist, and elastic center is taken after Jonkman et al. [23]. The blades are developed using elastic beam-column elements that require cross-sectional area (*A*), young's modulus (*E*), shear modulus (*G*), and moments of inertia (I_y, I_z, and *J*) to define the structural mass and stiffness.

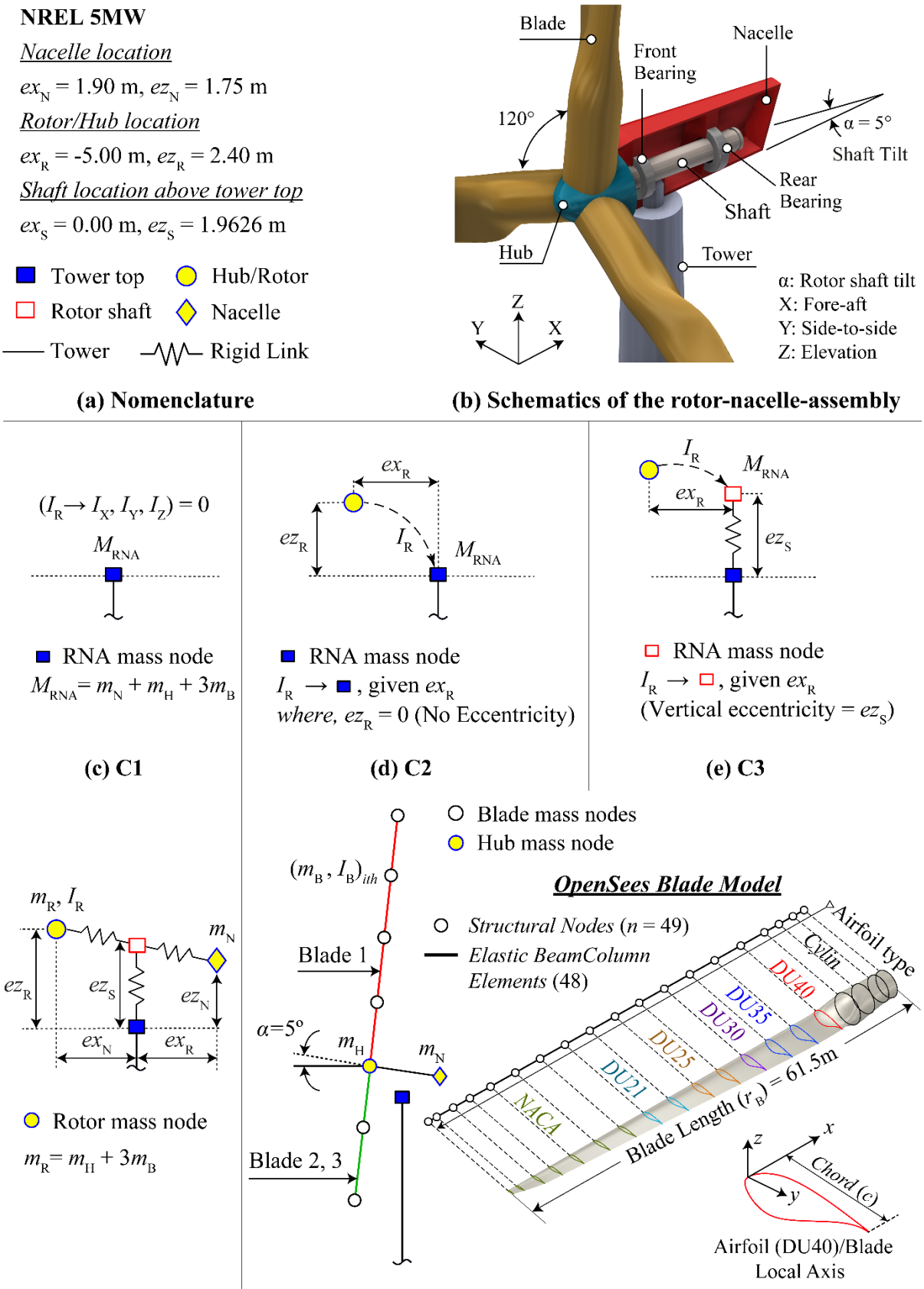

Figure 3 (a) Nomenclature of the quantities used for rotor-inertia modeling; (b) Schematic description of rotor-nacelle-assembly (RNA); RNA configuration with (c) no eccentricity and

no rotary inertia of blades; (d) rotary inertia but no eccentricity; (e) rotary inertia with vertically-eccentric RNA; (f) disintegrated nacelle and rotor with horizontal and vertical eccentricity; (g) disintegrated nacelle, hub, and fully modeled blades

I_y and I_z is the moment of inertia about the local y-axis and z-axis of the blade, respectively, and J is its torsional moment of inertia. The difference between the global axis of the wind turbine and the local axis of the blade is further clarified in Figure 4.

A typical design of a wind turbine blade involves a complex fusion of composite materials [49–51]. In this study, a uniform material is assumed for the blade. The input parameters for the blade elements are obtained using a genetic algorithm-based optimization [52–54]; an efficient method adopted in various studies for the shape and performance optimization of the composite blades [55] and OWT towers [56], respectively. The objective and outcome of the optimization process are summarised here for brevity. The blade optimization is performed to obtain cross-sectional thickness (t), the slope of thickness change along the blade (S), material density (ρ), Young's modulus of a uniform-anisotropic material (E_y and E_z), and shear modulus (G). It may be noted that OpenSees does not allow the use of bi-directional E in the elastic beam elements, therefore, the material anisotropicity is introduced by scaling I_z of each blade element with a ratio E_z/E_y. The optimized properties are used to calculate the mass, stiffness, and in turn, the modal frequencies of the blade that are similar to the NREL 5MW blade [23]. The values of t, S, ρ, E_y, E_z, and G used in this study are 26.79 mm, 3.156×10^{-4}, 1893 kg/m^3, 40.015 GPa, 9.203 GPa, and 6.053 GPa, respectively [48].

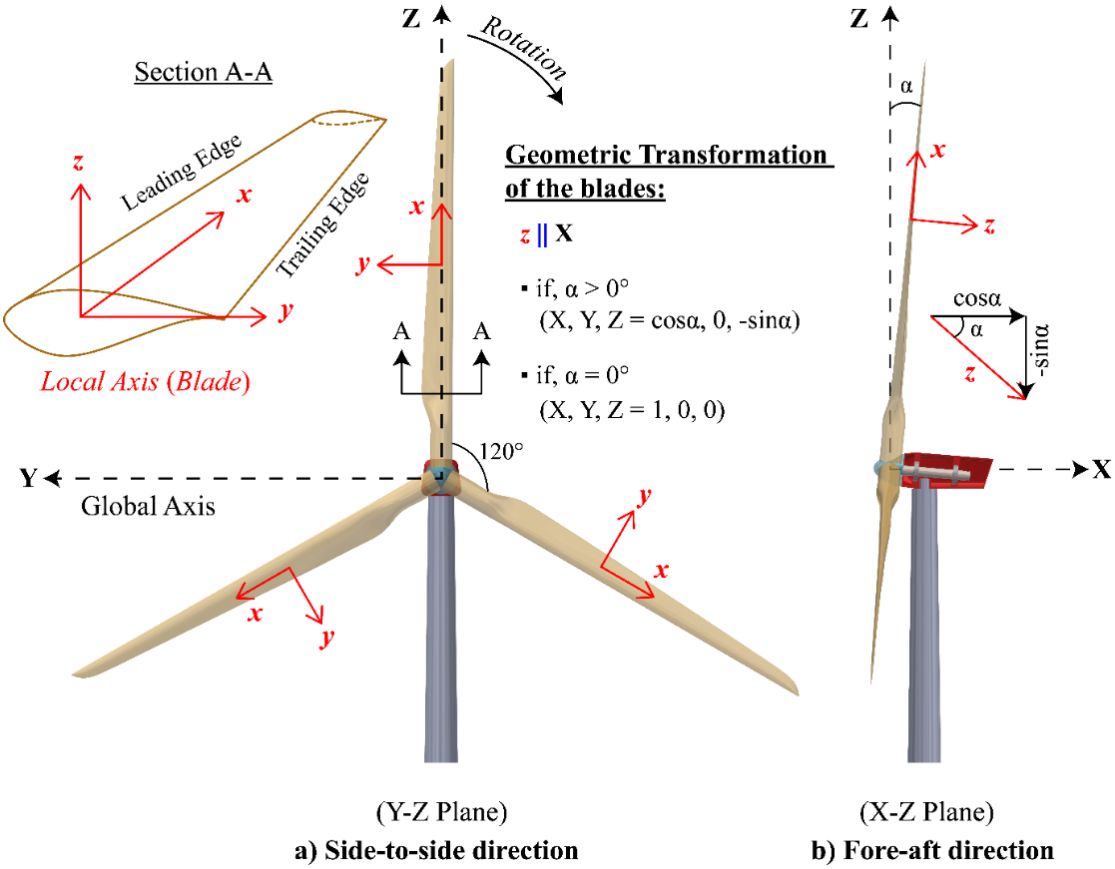

Figure 4 Geometric transformation of the blade's local axis to the global axis, (a) side-to-side; (b) fore-aft direction

2.2.2. Geometric transformation of the blades

Figure 4 shows the local and global coordinate systems used for the blades and the wind turbine, respectively. Element stiffness and resisting forces must be transformed from the local axes to the global system, for all structural components, for a reliable numerical analysis. This is achieved by using appropriate coordinate-transformation in OpenSees [29,57]. The geometric transformation is straightforward for the supporting tower. For blades, the orientation of the local axes may depend on the angle of the shaft tilt (α). For instance, the local *z*-axis of each blade will be parallel to the global X-axis if α is zero. But, if α is greater than zero, the local system of the axis will be rotated accordingly, shown in Figure 4. In this study, the rotor shaft tilt (α) of 0.5º is used [23], forming the coordinate transformation shown in Figure 4b and thus, applied in the blade-integrated rotor configuration of the OWT, i.e., C5 as discussed in the previous section.

3. Vulnerability assessment

3.1. Earthquake records

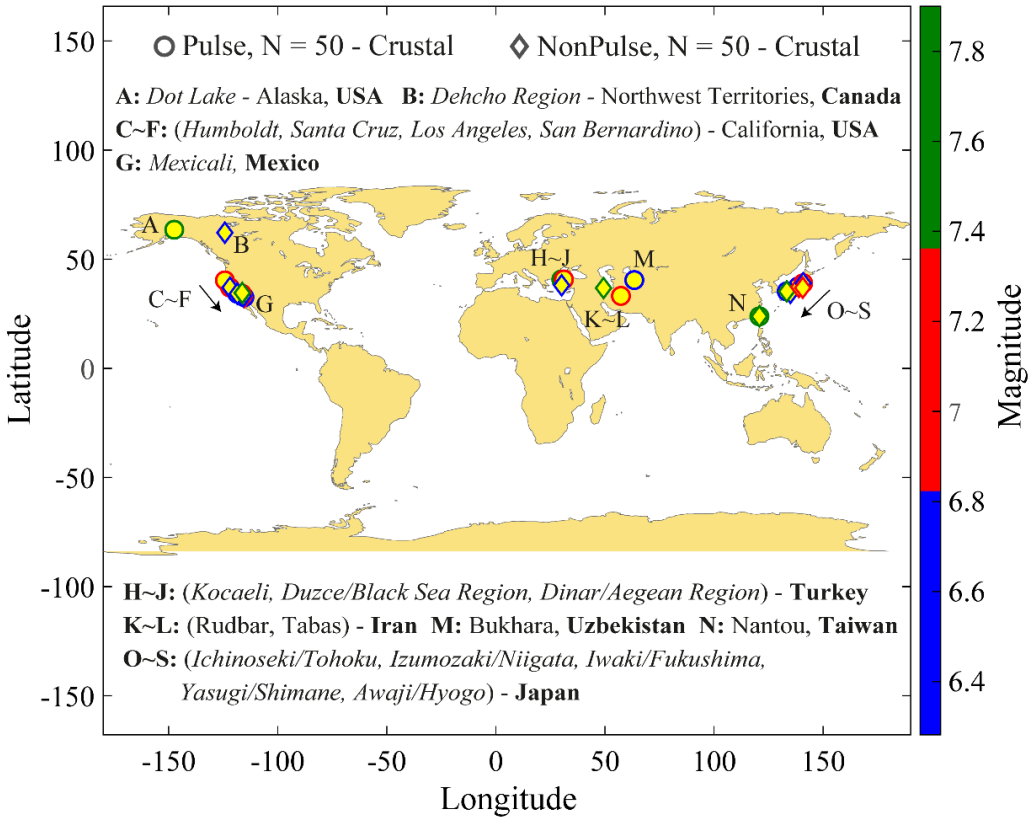

Figure 5 Epicentral locations of crustal records, selected for nonlinear dynamic analysis

Earlier research has shown the prominent seismic vulnerability of offshore wind turbines to crustal earthquakes, having peak ground velocity (*PGV*) > 30 cm/s, and strong vertical accelerations [5]. Such records will probably be a viable choice to achieve the system collapse

in this study and quantify the seismic fragilities as a function of rotor-inertia configurations, explained earlier in Section 2.2. Figure 5 shows the epicentral locations of the selected shallow crustal records that include Dot Lake Alaska United States (US), Petrolia California (US), Los Angeles (US), Kocaeli (Turkey), Rasht (Iran), Nantou (Taiwan), Osaka (Japan), Tohoku (Japan), etc. Most of these locations are potential sites for offshore wind farm installations. Thus, a total of 100 shallow crustal records are selected from the Next Generation Attenuation (NGA) database and the strong motion records set developed by Foulser-Piggott and Goda [58]. The selected records are further sub-divided into pulse-like and non-pulse-like categories following the pulse identification method proposed by Chang et al. [59,60]. This is done to further understand whether the pulse energy influences the failure probabilities of OWTs analyzed under different levels of rotor simplifications.

The records are selected within 6.0 - 8.0 magnitude (M) and source-to-site distance (R) of up to 35km, having a minimum PGA and PGV of 0.1 g and 30 cm/s, respectively (refer to Appendix for more details). The mean PGA and PGV for the pulse-like recordset is 0.452 g and 68.38 cm/s, whereas these values correspond to 0.465 g and 46.64 cm/s for the non-pulse-like records. Figure 6 shows the log-scale response spectra of the three components (two horizontal and one vertical) of the two recordsets along with their median and the 16th and 84th percentiles.

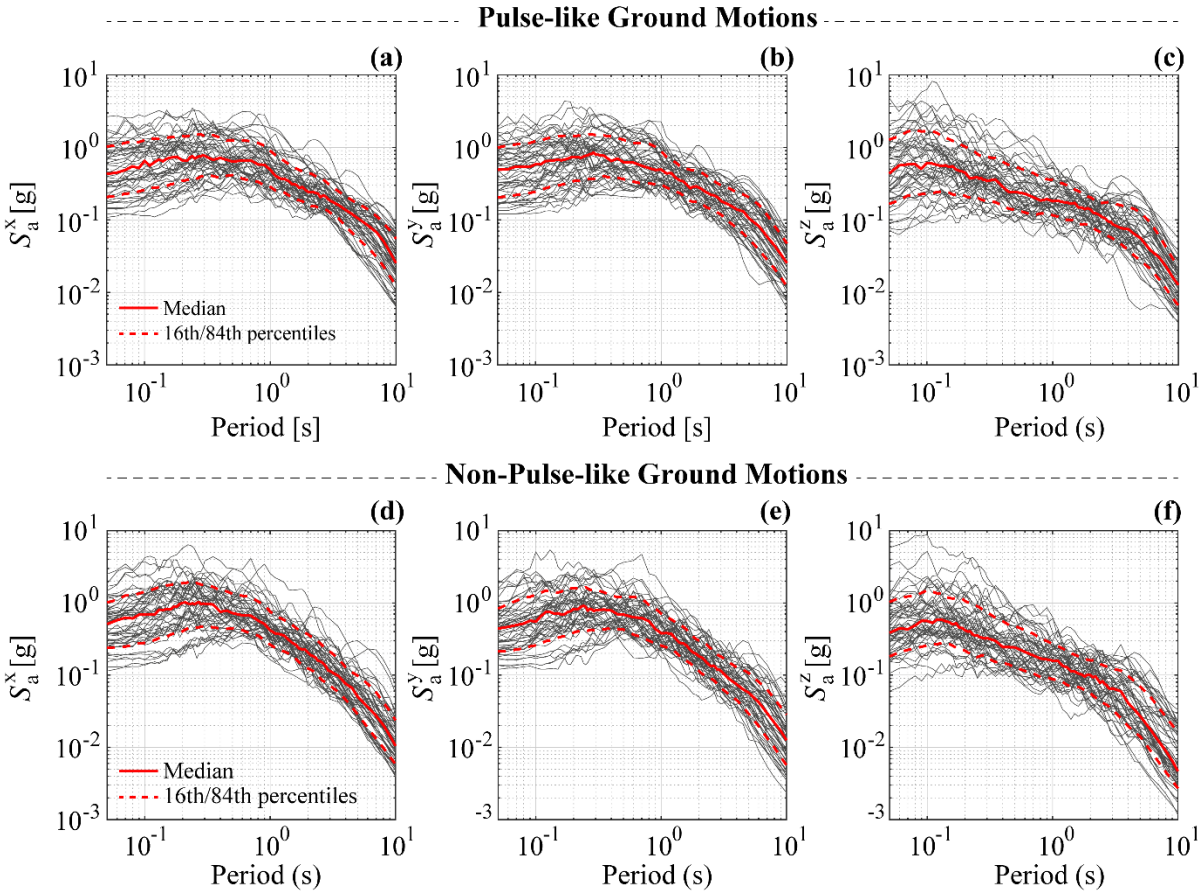

Figure 6 Response spectra of the horizontal and vertical crustal ground motions, (a-c) pulse-like ground motions; (d-f) non-pulse-like ground motions

3.2. Structural analysis

Two types of structural analyses are performed for the five structural models (C1 to C5), i.e., modal analysis, and nonlinear time history analysis. The modal analysis is performed to evaluate their vibration periods and to understand their dynamic behavior. The nonlinear time-history analyses are conducted to determine the structural response under static and dynamic loads considered in this study.

3.2.1. Nonlinear time-history analysis

The unscaled ground motions are applied in conjunction with the static wind, wave, and inertial loads during the nonlinear dynamic analysis. For the given sets of the selected records, 100 response history analyses are performed for each structural model, thus a total of 500 analyses in this study. The total system damping of 3% is often adopted for nonlinear dynamic analysis of OWTs in the earlier studies [2,5]. Using the same damping value, the present work utilizes the Rayleigh damping model for the first three bending modes of the tower, which is analogous to the choice for conventional structures, where the first three modes are in pairs. Moreover, the Newton-Raphson method is used for numerical integration. The initial time increment is set according to the ground motion time-step, which is allowed to iteratively decompose into a smaller value to achieve convergence [57].

3.3. Fragility Analysis

In performance-based earthquake engineering, the structural responses are estimated in terms of an engineering demand parameter (EDP) via nonlinear response history analysis for a representative set of earthquake intensities [61]. The probabilities of an EDP exceeding a prescribed damage level, i.e., limit state (LS), as a function of a ground motion intensity measure (*IM*) is obtained by fragility analysis [27,62,63].

3.3.1. EDP and limit states

In this study, the demand-to-capacity ratio (Y) is defined as the EDP of interest and is evaluated for two limit states, i.e., the serviceability limit state (SLS) and the ultimate limit state (ULS). The SLS is taken as the maximum tower top rotation of ±0.5°, which is the recommended guideline by Det Norske Veritas (DNV) for monopile foundations [64]; however, it is also described as a criterion in the literature for the tower or nacelle level rotations [2,5,65]. The ULS is followed after the strength and stability check for thin-walled shells in Annex D of the Part 1-6 of the Eurocode 3 [66]. The tower strength is assured as the maximum of the von-mises equivalent design stress (σ_{eq}) and the buckling strength through stress limitation, expressed as demand (D) to capacity (C) ratios Y_v and Y_b, respectively, as below.

$$Y_{ULS} = \max\{Y_v, Y_b\} \tag{5}$$

$$Y_v = D/C = \sigma_{eq}/f_y = \sqrt{\sigma^2 + 3.\tau^2}/f_y \leq 1 \tag{6}$$

$$Y_b = \left(\sigma/\sigma_{x,Rd}\right)^{k_x} + \left(\tau/\tau_{x\theta,Rd}\right)^{k_\tau} \leq 1 \tag{7}$$

where, f_y is the steel yield strength (S355 = 355 MPa). σ and τ are the meridional (compressive) and planar shear stress demands on the tower, transition piece, and the monopile (see De Risi et al. [2] for more details). $\sigma_{x,Rd}$ and $\tau_{x\theta,Rd}$ are the corresponding capacities which along with the factors k_x and k_τ are detailed in Annex D of the Eurocode 3 [66].

3.3.2. Intensity measure and fragility modeling

In this study, fragility curves are obtained by estimating the conditional probabilities (p) of the EDP at the desired limit states (Y_{LS} >1), described above, as a function of an earthquake intensity measure (IM) using the following expressions.

$$p[Y_{LS} > 1|IM, \chi] = \Phi\left[\ln \eta_{Y_{LS}|IM} / \beta_{Y_{LS}|IM}\right] \tag{8}$$

$$\ln \eta_{Y_{LS}|IM} = \ln a + b \ln IM \tag{9}$$

$$\beta_{Y_{LS}|IM} = \sigma_{\ln Y_{LS}|IM} = \sqrt{\sum_{i=1}^{N} \left(\ln Y_{LS,i} - \ln \eta_{Y_{LS}|IM_i}\right)^2 \Big/ (N-2)} \tag{10}$$

$$IM = S_a^{xyz}(T_1) = [S_a^x(T_1^x) \cdot S_a^y(T_1^y) \cdot S_a^z(T_1^z)]^{1/3} \tag{11}$$

Equation 8 describes a three-parameter fragility model including Φ, χ, and $\beta_{Y_{LS}|IM}$ [27]. Φ $(\cdot)$ is the standardized cumulative distribution function (CFD). The second parameter is a vector, $\chi = [\ln a, b, \beta_{Y_{LS}|IM}]$, comprising of statistical elements that help analyse the efficiency of a potential IM. The values of these elements result from the probabilistic linear regression, defined using equation (9) and (10), on the calculated response $[Y_{LS,i},\ i = 1{:}N]$ for a suite of N ground motions and corresponding values of the $IM = [IM_i, i = 1{:}N]$. The third parameter, $\beta_{Y_{LS}|IM}$, is the standard deviation of Y_{LS} at the given IM. In this study, the geometric mean of the first mode spectral accelerations in all three directions, $S_a^{xyz}(T_1)$, is used as the IM due to its efficiency in representing the structural response for onshore [7] and offshore wind turbines [5], particularly when earthquake records contain significant vertical accelerations.

4. Results and discussions

4.1. Mode shapes and participation masses

Eigenvalue analysis is conducted to identify the difference in dynamic characteristics of OWTs with various RNA configurations (C1 to C5), as explained earlier in Section 2.2. The tower mode shapes are identical for all RNA models, as shown in Figure 7, along with the vibration periods (T) in all three directions for the first-four tower modes. In the case of lumped mass RNA models, i.e., C1 to C4, the inclusion of rotary inertia increases the T-values (X and Y), more prominently at higher modes. C5 undergoes a mixed dynamic behavior. The first mode (T_1) response is similar to C3 and C4, whereas the higher modes are closer to C1. This may be due to the effects of blades' deformability on the tower modes, which is absent in a lumped mass model that intrinsically considers blades as a rigid body. As shown earlier in Figure 3(c&g), C1 ignores the rotational inertia (I_R) of the RNA, and C5 introduces it explicitly as the

cross-sectional inertia of the blades (I_B) that decreases gradually away from the blade root, leading to a non-uniform distribution of the inertia along the blade length (r_B). Thus, the higher I_B at the blade root in C5 tends to imitate the tower response that is similar to C3 and C4. Also, the lowering of I_B towards the blades' tip may cause rotary inertia at the tower in C5 closer to C1, resulting in nearly identical higher-mode dynamic response.

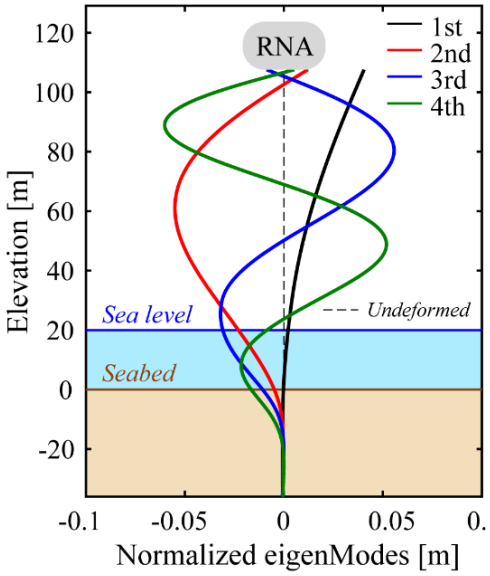

Vibration periods (T) for the first four tower modes in all directions

Mode	C1			C2			C3		
	X	Y	Z	X	Y	Z	X	Y	Z
1st	3.842	3.842	0.153	3.881	3.917	0.153	3.979	4.016	0.153
2nd	0.550	0.550	0.068	0.652	0.759	0.068	0.664	0.764	0.068
3rd	0.225	0.225	0.035	0.328	0.370	0.035	0.323	0.364	0.035
4th	0.115	0.115	0.024	0.177	0.183	0.024	0.175	0.181	0.024

Mode	C4			C5		
	X	Y	Z	X	Y	Z
1st	3.981	4.015	0.153	3.972	3.983	0.151
2nd	0.671	0.765	0.068	0.596	0.535	0.068
3rd	0.328	0.364	0.035	0.205	0.265	0.035
4th	0.176	0.181	0.024	0.135	0.120	0.024

[T : in seconds]

Figure 7 First four normalized tower mode shapes, generic to all RNA configurations, and their natural periods in all three directions

This analogy is further explained in terms of participation masses (*PM*), shown in Figure 8. C1 to C4 shows a uniform distribution of active *PM* in translational X, Y, and Z-direction, where the X and Y tower modes are coincident in pairs. The effects of rotary inertia and rotor eccentricity reduce the active masses at each mode and delay achieving over 90% *PM* in all three directions. In the case of C5, the active *PM* at each tower mode is analogous to the other cases; however, their occurrence is significantly delayed due to the presence of local blade modes. The first-order tower and blade mode shapes and vibration periods (T) are further shown in Figure 9, which are in good agreement with [23,28]. Thus, it takes 19, 22, and 65 modes to obtain nearly 100%, 100%, and 90% *PM* in X, Y, and Z-direction for C1, C2 to C4, and C5, respectively. Besides, the vertical vibrations of OWTs are insensitive to the effects of rotary inertia and rotor eccentricity, in this study.

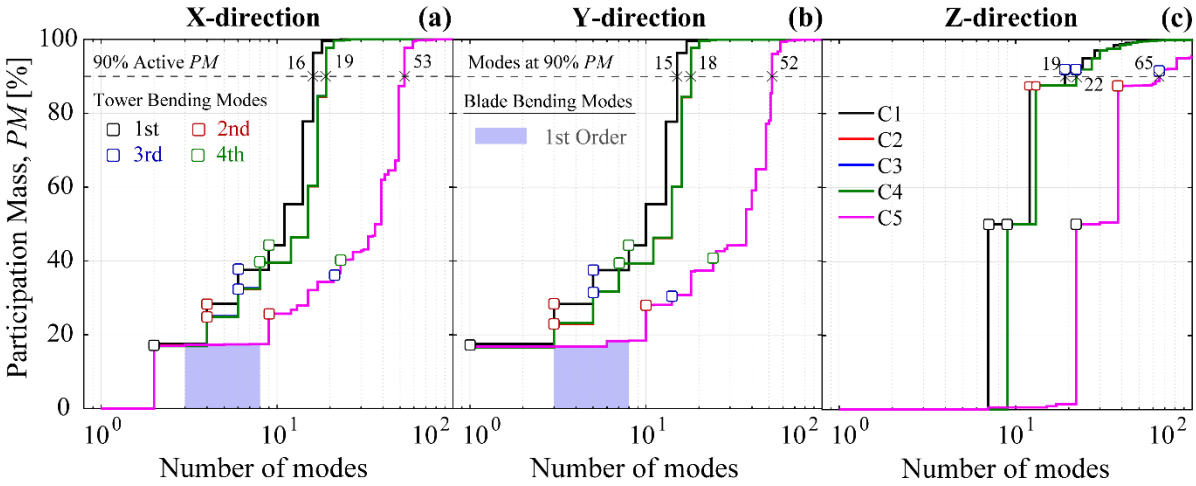

Figure 8 Distribution of the participation masses for the five RNA configurations, (a) X-direction; (b) Y-direction; (c) Z-direction

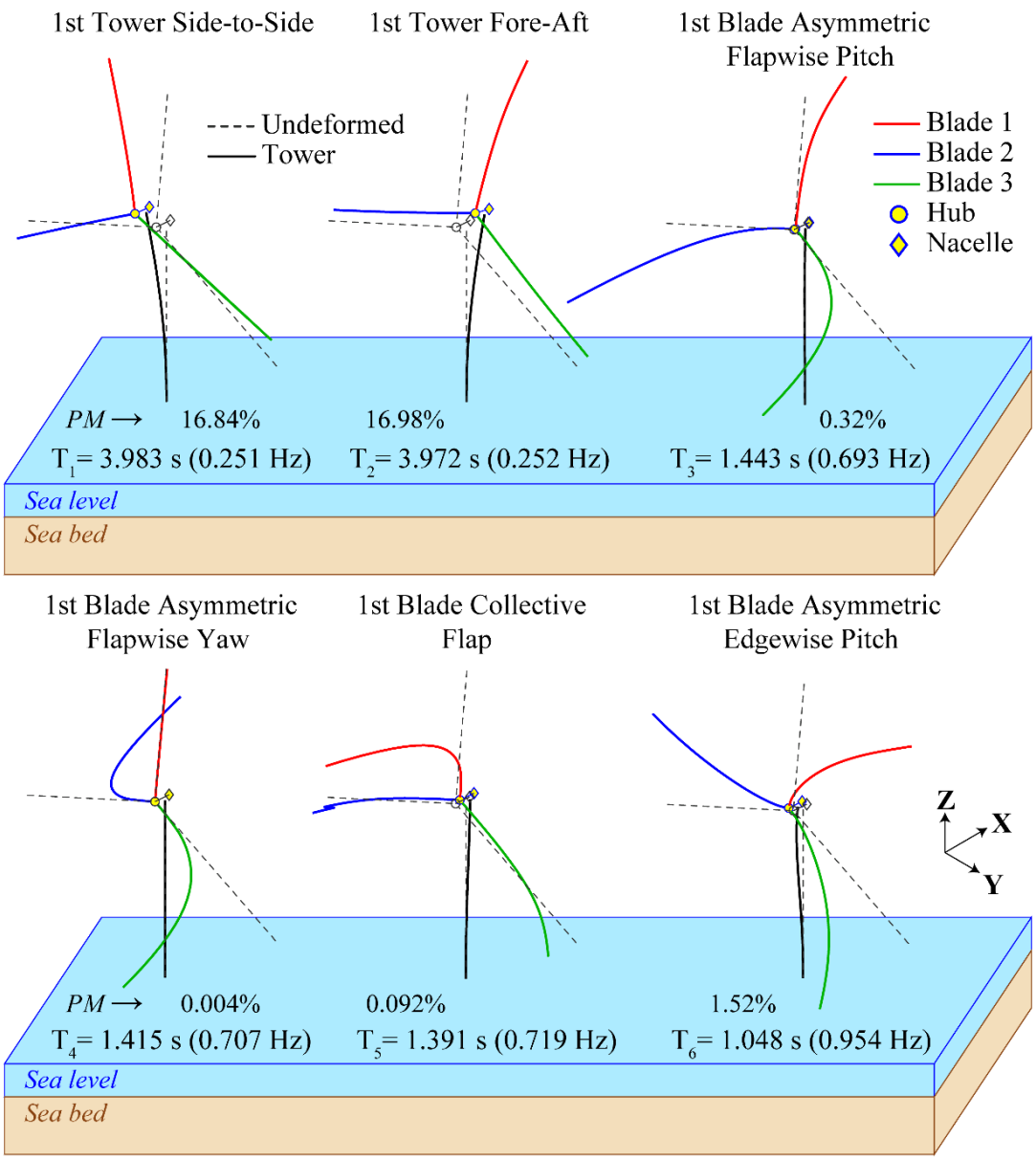

Figure 9 First-order tower and blade modes

4.2. Tower stress and displacement response

The effects of rotary inertia and rotor eccentricity on the tower failure are examined based on the normalized tower stress (Y_{ULS}) profiles. Figure 10 shows the Y_{ULS} profiles for a pulse-like and a non-pulse-like record, as representative of those, that exceeded the ULS. These have been recorded in Tabas (Iran) and Tohoku (Japan) and their magnitude (M), rupture distance (R), peak ground acceleration (PGA) as well as peak ground velocity (PGV) are shown in Figure 10 (a) and (b), respectively. Since the ULS criterion (Equation (5)) is driven by the buckling strength of a hollow cylindrical shell, the zones of the tower length, where Y_{ULS} >1, represent a failure by compression (buckling) [2,5].

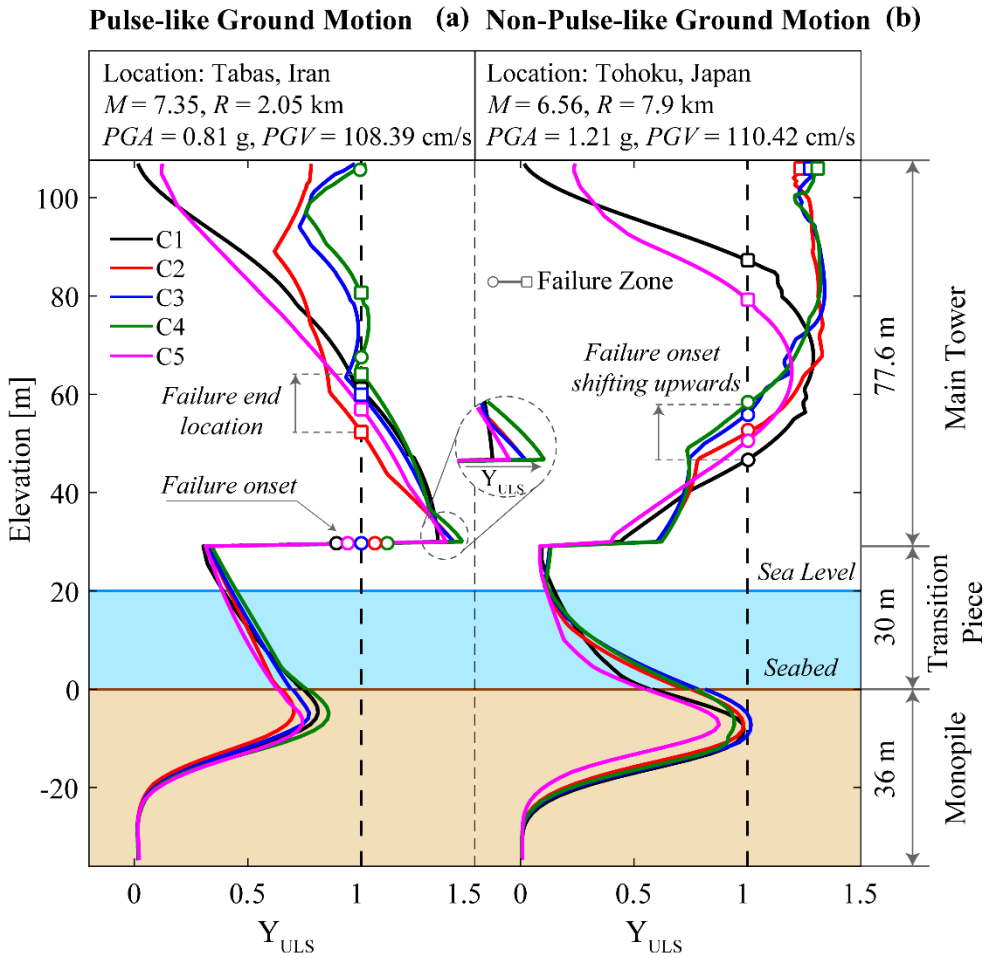

Figure 10 Normalized tower stress profiles, showing failure zones at ULS, under crustal records, (a) pulse-like ground motion; (b) non-pulse-like ground motion

Figure 10(a & b) shows that the tower failure zones can vary under different earthquake records. This is in agreement with previous studies and has been associated with the strength of vertical excitations in a record, regardless of the pulse presence [5]. It is noteworthy that for all RNA configurations (C1 to C5), the failure occurs at the main tower base above the transition piece Figure 10(a). The Y_{ULS} profiles for C1 and C5 show a first-mode response, where C1 ignores the rotary inertia (I_R) and the RNA eccentricity and C5 considers fixed root flexible blades. However, for other lumped mass RNA models (C2 to C4), the tower tends to depict a higher mode response and additionally fails near the upper-mid and the top. Moreover, the effects of I_R and eccentricity increases the Y_{ULS} value at the failure onset and changes the failure end location. In the case of Tohoku, Figure 10(b), the failure initiates below the mid-tower length, and it appears to shift towards the slenderer part of the tower, i.e., upwards, due to rotary inertia and rotor eccentricity. Once again, the stress profiles for C1 and C5 are similar but differ from C2 to C4 that are mutually comparable. The failure zone for C1 is larger than C5, and it lies between the lower-mid to upper-mid tower length. The failure zone for C2 to C4 ranges from the lower-mid tower length and leads up to the top which can be attributed to the difference in their high-mode natural frequencies of vibration from C1 and C5 [6].

It can also be observed that the tower response for C5, under both records, lies between the C1 and C4 which infers that tower stresses are partially dissipated by the flexibility of the blades.

This is due to the presence of the local blade modes in C5 that gradually activate the inertia of the flexible blade at higher modes; a phenomenon that is discussed earlier in Section 4.1 using the modal analysis results. This is further explained in terms of tower displacement. Figure 11 shows the tower chord rotation (θ) history in the fore-aft (X) and side-to-side (Y) direction, under the record for which the Y_{ULS} profile is shown in Figure 10(a). For clarity, θ_X and θ_Y time-history are shown between 15 and 25 seconds of the record. In both directions (X and Y), the C5 remains between the non-eccentric (C1 and C2) and eccentric RNA models (C3 and C4), where the latter has achieved the highest values of θ. This also indicates that the deformability of the blades helps damp out some displacement response of the tower under crustal earthquakes.

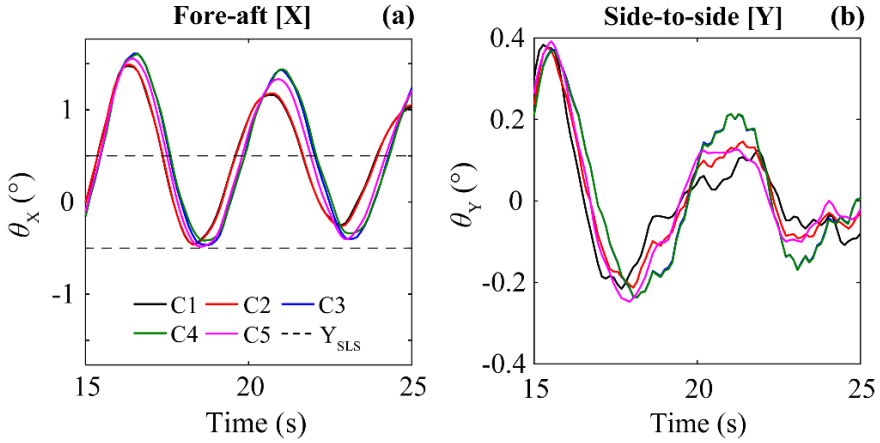

Figure 11 Displacement response of the OWT tower top, (a) fore-aft direction; (b) side-to-side direction

4.3. Seismic fragility curves

Figure 12 shows the seismic fragility curves of the OWT with five RNA configurations under pulse-like and non-pulse-like ground motions. The probabilities of the Y exceeding unity, ($p[Y_{LS}>1]$), at the SLS and ULS are shown. As shown in Figure 12(a & c), at a given value of $S_a^{xyz}(T_1)$ e.g., 0.1 g, $p[Y_{SLS}>1|0.1\text{ g}]$, the probability of exceeding the SLS is higher under pulse-like ground motions, where the rotary inertia has a slight-to-negligible influence on the seismic vulnerability of OWTs at the SLS. The fragility curves represent identical, yet high probabilities of reaching the SLS at relatively lower values of $S_a^{xyz}(T_1)$ than the ULS. It is shown in Figure 12(a & b) that the seismic vulnerability of OWTs at ULS is generally higher under pulse-like ground motions. However, it differs significantly when the rotary inertia is considered. The difference is more obvious under non-pulse-like ground motions, where at a given value of $S_a^{xyz}(T_1)$ e.g., 0.75 g, $p[Y_{ULS}>1|0.75\text{ g}]$ for C1 is 0.58, which increases to 0.75 when rotary inertia is introduced in C2. The value of $p[Y_{ULS}>1|0.75\text{ g}]$ further increases to 0.88 due to the influence of the vertical eccentricity (ez_S) of the RNA (C3), which remains unaffected by the additional horizontal eccentricity of the nacelle (ez_N) and the rotor (ez_R) in C4. Regardless of the ground motion type, the vulnerability of OWT with flexible blades (C5) is greater than C1 but less than C2 to C4. Thus, like the tower stress and displacement response, C5 offers an intermediate estimate of the failure probabilities of the OWT in shallow crustal regions.

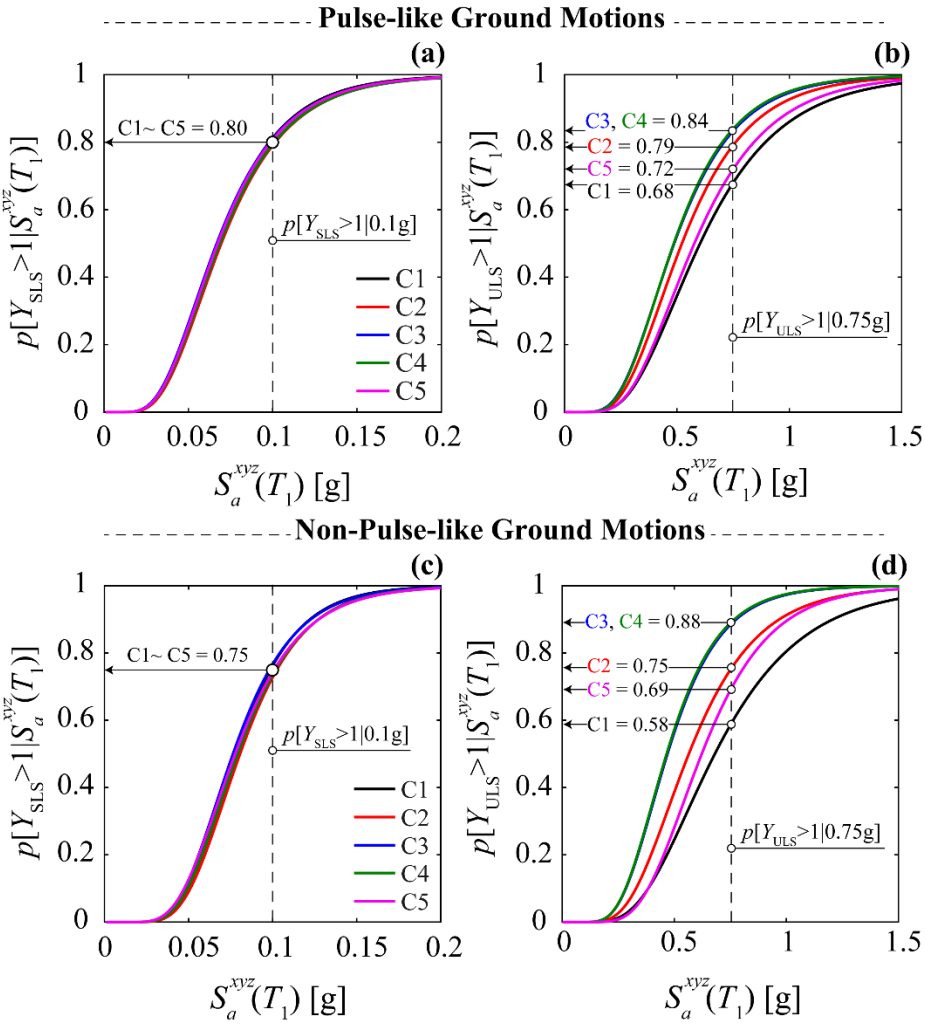

Figure 12 Influence of the earthquake type, rotary inertia, rotor eccentricity and blade flexibility on the failure probabilities of the 5MW OWT, (a,c) SLS; (b,d) ULS

5. Conclusions

Numerical simulations are vital to understanding the response of complex energy-related structures and are precursors to their reliable design. The rotor-nacelle-assembly (RNA), even though it is a critical component of a functional wind turbine, is often (over)simplified as a lumped mass for numerical seismic analysis of wind turbines. Such simplifications may include the exclusion of the rotary inertia effects of blades on the tower and RNA eccentricity, which can, in turn, affect our estimates for the seismic vulnerability of wind turbines, as RNA contributes significantly to the total system mass. Also, the lumped approach assumes the RNA as a single rigid body, ignoring the effects of the blades' deformability on the dynamic behavior that arises from their length and slender structural characteristics.

The present study discusses the effects of the three key RNA parameters, i.e., (i) rotary inertia of the blades, (ii) rotor eccentricity, and (iii) blades' flexibility, on the seismic performance of OWTs. Numerical analysis of the different degrees of refinement is implemented to investigate the influence of these parameters on the failure modes, their locations, and failure probabilities

of OWT towers under pulse-like and non-pulse-like shallow crustal earthquakes. The conclusions drawn from this study are as follows:

1. The rotary inertia of the blades and the rotor eccentricity lengthens the natural periods of vibration of the OWT and influences the modal participation factors, particularly that of the higher modes, in comparison to the model that neglects these two parameters, i.e. C1.
2. The vibration periods of the OWT with the full blades (C5) are greater than C1 but lower than the ones with rotary inertia (C2) and the vertical (C3) and the additional horizontal (C4) eccentricity of the RNA. This is due to the presence of the local blade modes in C5 that gradually activate the inertia of the flexible blade at higher modes.
3. The rotary inertia and rotor eccentricity tend to induce higher mode behavior in the tower and affect the failure onset and end locations, i.e., the failure zones in the tower.
4. When the failure initiates from the main tower base, the effects of rotary inertia and eccentricity increase the intensity of the failure (Y_{ULS}), and failure leads up to the mid-tower length. For the C3 and C4 cases, the tower damage can be localized at two additional locations due to the higher mode behavior, i.e., either at the tower top or at upper-mid tower length.
5. In case that the failure initiates around the mid-tower length, the onset location tends to shift up towards the slenderer section of the tower due to the inclusion of the blades' rotary inertia and the rotor eccentricity. Failure for C1 and C5 can last up to upper-mid tower length, whereas for C2 to C4 it can lead up to the tower top. This can be crucial for the design evaluations of the OWT towers in areas susceptible to shallow crustal earthquakes.
6. The tower failure profiles and displacement response of C5 lie within the range of C1 and C4. This is because the higher mode behavior in C5 is not as pronounced as the rigid-body inertia RNA configurations (C2 to C4), due to the presence of local blade modes.
7. The allowable tower top deformations are insensitive to the consideration of rotary inertia, the rotor eccentricity, and the blade deformability. However, at the ultimate limit state (ULS), the OWT that considers the rotary inertia with eccentric RNA (C3, C4) shows the highest probability of the tower failure, which is considerably lower when the combined effect of these two parameters is ignored (C1).
8. The effects of deformable blades reduce the estimated seismic vulnerability of OWT, but it is considerably greater than C1. This is because the blades' flexibility damps out the seismic demand on the tower. Thus, it can be anticipated that the blades may damage if subjected to excessive excitations. This requires the use of nonlinear blade material and should be treated as a potential future development.
9. Moreover, OWTs have shown a higher probability of failure under pulse-like ground motions; however, it can be slightly lower than non-pulse-like ground motions for C3 and C4.

The above observations lead to the general conclusion that the lack of accurate consideration of blades and the RNA mass eccentricity may dominate the prediction of failure modes at different tower sections. The seismic vulnerability of the OWTs can be underestimated, at least in areas of shallow crustal earthquakes, if these parameters are ignored. The failure probabilities may also be overestimated if the deformability of the blades is ignored. In this

study, a constant damping value of 3% is adopted for all structural modes, which can be higher for the local blade modes, and it may further influence the structural response of OWTs. Further studies are required, encompassing more refined models to examine the effects of modal and radiation damping, kinematic soil-pile interaction, as well as the effect of potential blade damage on the seismic vulnerability of OWTs.

Acknowledgments

The second and third author acknowledges the support from the Engineering and Physical Sciences Research Council (EPSRC) project UKCRIC (EP/R012806/1). The earthquake ground motion data, used in this study, were obtained from the K-NET and KiK-net database (http://www.kyoshin.bosai.go.jp/), the SK-net (http://www.sknet.eri.u-tokyo.ac.jp/), and the PEER-NGA database (http://peer.berkeley.edu/nga/index.html). The numerical simulations were carried out using the computational facilities of the Advanced Computing Research Centre, University of Bristol (http://www.bris.ac.uk/acrc/).

References

1. Prowell I, Veletzos M, Elgamal A, Restrepo J. Experimental and numerical seismic response of a 65 kW wind turbine. *Journal of Earthquake Engineering* 2009; **13**(8): 1172–1190.
2. De Risi R, Bhattacharya S, Goda K. Seismic performance assessment of monopile-supported offshore wind turbines using unscaled natural earthquake records. *Soil Dynamics and Earthquake Engineering* 2018; **109**: 154–172.
3. Alati N, Failla G, Arena F. Seismic analysis of offshore wind turbines on bottom-fixed support structures. *Phil Trans R Soc A* 2015; **373**(2035): 20140086.
4. Ma H, Yang J, Chen L. Numerical analysis of the long-term performance of offshore wind turbines supported by monopiles. *Ocean Engineering* 2017; **136**(January): 94–105.
5. Ali A, De Risi R, Sextos A, Goda K, Chang Z. Seismic vulnerability of offshore wind turbines to pulse and non-pulse records. *Earthquake Engineering & Structural Dynamics* 2020; **49**(1): 24–50.
6. Nuta E, Christopoulos C, Packer JA. Methodology for seismic risk assessment for tubular steel wind turbine towers: application to Canadian seismic environment. *Canadian Journal of Civil Engineering* 2011; **38**(3): 293–304.
7. Sadowski AJ, Camara A, Málaga-Chuquitaype C, Dai K. Seismic analysis of a tall metal wind turbine support tower with realistic geometric imperfections. *Earthquake Engineering & Structural Dynamics* 2017; **46**(2): 201–219.
8. Zhao Z, Dai K, Camara A, Bitsuamlak G, Sheng C. Wind Turbine Tower Failure Modes under Seismic and Wind Loads. *Journal of Performance of Constructed Facilities* 2019; **33**(2): 04019015.
9. Wang S, Kutter BL, Chacko MJ, Wilson DW, Boulanger RW, Abghari A. Nonlinear Seismic Soil-Pile Structure Interaction. *Earthquake Spectra* 1998; **14**(2): 377–396.
10. Boulanger RW, Curras CJ, Kutter BL, Wilson DW, Abghari A. Seismic Soil-Pile-Structure Interaction Experiments and Analyses. *Journal of Geotechnical and Geoenvironmental Engineering* 1999; **125**(9): 750–759.
11. El Naggar MH, Bentley KJ. Dynamic analysis for laterally loaded piles and dynamic p-y curves. *Canadian Geotechnical Journal* 2000; **37**(6): 1166–1183.
12. El Naggar MH, Shayanfar MA, Kimiaei M, Aghakouchak AA. Simplified BNWF

model for nonlinear seismic response analysis of offshore piles with nonlinear input ground motion analysis. *Canadian Geotechnical Journal* 2005; **42**(2): 365–380.
13. Barari A, Bagheri M, Rouainia M, Ibsen LB. Deformation mechanisms for offshore monopile foundations accounting for cyclic mobility effects. *Soil Dynamics and Earthquake Engineering* 2017; **97**(February): 439–453.
14. Luo C, Yang X, Zhan C, Jin X, Ding Z. Nonlinear 3D finite element analysis of soil-pile-structure interaction system subjected to horizontal earthquake excitation. *Soil Dynamics and Earthquake Engineering* 2016; **84**: 145–156.
15. Cuéllar P, Mira P, Pastor M, Fernández Merodo JA, Baeßler M, Rücker W. A numerical model for the transient analysis of offshore foundations under cyclic loading. *Computers and Geotechnics* 2014; **59**: 75–86.
16. Kourkoulis Ã RS, Lekkakis PC, Gelagoti FM, Aynia AMK. Suction caisson foundations for offshore wind turbines subjected to wave and earthquake loading: effect of soil-foundation interface 2014; **64**(3): 171–185.
17. Gelagoti F, Georgiou I, Kourkoulis R, Gazetas G. Nonlinear lateral stiffness and bearing capacity of suction caissons for offshore wind-turbines. *Ocean Engineering* 2018; **170**: 445–465.
18. Esfeh PK, Kaynia AM. Earthquake response of monopiles and caissons for Offshore Wind Turbines founded in liquefiable soil. *Soil Dynamics and Earthquake Engineering* 2020; **136**: 106213.
19. Kampitsis AE, Sapountzakis EJ, Giannakos SK, Gerolymos NA. Seismic soil-pile-structure kinematic and inertial interaction-A new beam approach. *Soil Dynamics and Earthquake Engineering* 2013; **55**: 211–224.
20. Lesgidis N, Sextos A, Kwon OS. A frequency-dependent and intensity-dependent macroelement for reduced order seismic analysis of soil-structure interacting systems. *Earthquake Engineering & Structural Dynamics* 2018; **47**(11): 2172–2194.
21. De Biasio M. Ground motion intensity measures for seismic probabilistic risk analysis. Civil Engineering. Université de Grenoble, 2014.
22. Lee TH, Mosalam KM. Probabilistic Seismic Evaluation of Reinforced Concrete Structural Components and Systems. *PEER Report 2006/04* 2006.
23. Jonkman J, Butterfield S, Musial W, Scott G. Definition of a 5-MW Reference Wind Turbine for Offshore System Development 2009(February).
24. Arany L, Bhattacharya S, Macdonald JHG, Hogan SJ. Closed form solution of Eigen frequency of monopile supported offshore wind turbines in deeper waters incorporating stiffness of substructure and SSI. *Soil Dynamics and Earthquake Engineering* 2016; **83**: 18–32.
25. Patil A, Jung S, Kwon OS. Structural performance of a parked wind turbine tower subjected to strong ground motions. *Engineering Structures* 2016; **120**: 92–102.
26. Dai K, Sheng C, Zhao Z, Yi Z, Camara A, Bitsuamlak G. Nonlinear response history analysis and collapse mode study of a wind turbine tower subjected to tropical cyclonic winds. *Wind and Structures* 2017; **25**(1): 79–100.
27. Jalayer F, Ebrahimian H, Miano A, Manfredi G, Sezen H. Analytical fragility assessment using unscaled ground motion records. *Earthquake Engineering and Structural Dynamics* 2017; **46**(15): 2639–2663.
28. Jonkman J, Musial W. Offshore code comparison collaboration (OC3) for IEA Wind Task task 23 offshore wind technology and deployment. *IEA Task 23* 2010; **303**(December): 74.
29. McKenna F. OpenSees: a framework for earthquake engineering simulation. *Computing in Science & Engineering* 2011; **13**(4): 58–66.
30. Batdorf SB. A Simplified Method of Elastic-Stability Analysis for Thin Cylindrical

Shells I - Donnell's Equation. *NACA Technical Note 1341* 1947.
31. American Petroleum Institute. Recommended Practice for Planning, Designing and Constructing Fixed Offshore Platforms — Working Stress Design. *API Recommended Practice* 2007; **24-WSD**(December 2000): 242.
32. Mosher RL. *Load-Transfer Criteria for Numerical Analysis of Axially Loaded Piles in Sand. Part 1. Load-Transfer Criteria.* 1984.
33. Vijayvergiya VN. Load-movement characteristics of piles. *4th Symp. of Waterway, Port, Coastal and Ocean Div., ASCEean Div., ASCE*, vol. 2, 1977.
34. Pisanò F, Jeremić B. Simulating stiffness degradation and damping in soils via a simple visco-elastic-plastic model. *Soil Dynamics and Earthquake Engineering* 2014; **63**: 98–109.
35. Kementzetzidis E, Metrikine A, Versteijlen W, Pisanò F. Frequency effects in the dynamic lateral stiffness of monopiles in sand: insight from field tests and 3D FE modelling. *Géotechnique* 2020: 1–43.
36. Kementzetzidis E, Corciulo S, Versteijlen WG, Pisanò F. Geotechnical aspects of offshore wind turbine dynamics from 3D non-linear soil-structure simulations. *Soil Dynamics and Earthquake Engineering* 2019; **120**: 181–199.
37. Corciulo S, Zanoli O, Pisanò F. Transient response of offshore wind turbines on monopiles in sand: role of cyclic hydro–mechanical soil behaviour. *Computers and Geotechnics* 2017; **83**: 221–238.
38. ASCE/SEI 7-10. Minimum Design Loads for Buildings and Other Structures: Second Printing 2010.
39. IEC 61400-1. *Wind Turbines-Part 1: Design Requirements*. International Electrotechnical Commission Geneva, Switzerland; 2005.
40. Frohboese P, Schmuck C. Thrust coefficients used for estimation of wake effects for fatigue load calculation. *European Wind Energy Conference*, 2010.
41. Arany L, Bhattacharya S, Macdonald J, Hogan SJ. Design of monopiles for offshore wind turbines in 10 steps. *Soil Dynamics and Earthquake Engineering* 2017; **92**(September 2016): 126–152.
42. Hussien MN, Karray M, Tobita T, Iai S. Kinematic and inertial forces in pile foundations under seismic loading. *Computers and Geotechnics* 2015; **69**: 166–181.
43. Di Laora R, Mylonakis G, Mandolini A. Pile-head kinematic bending in layered soil. *Earthquake Engineering & Structural Dynamics* 2013; **42**(3): 319–337.
44. Nikolaou S, Mylonakis G, Gazetas G, Tazoh T. Kinematic pile bending during earthquakes: analysis and field measurements. *Géotechnique* 2001; **51**(5): 425–440.
45. Kim DH, Lee SG, Lee IK. Seismic fragility analysis of 5MW offshore wind turbine. *Renewable Energy* 2014; **65**: 250–256.
46. Mylona EK V., Sextos AG, Mylonakis GE. Rotational seismic excitation effects on CIDH pile-supported bridge piers. *Engineering Structures* 2017; **138**: 181–194.
47. Gere JM, Goodno BJ. *Mechanics of Materials*. 8th ed. Cengage Learning, Boston, MA; 2012.
48. Ali A, De Risi R, Sextos A. Finite element modeling optimization of wind turbine blades from an earthquake engineering perspective (Under Review). *Engineering Structures* 2019.
49. Resor BR. Definition of a 5MW/61.5 m wind turbine blade reference model. *Albuquerque, New Mexico, USA, Sandia National Laboratories, SAND2013-2569 2013* 2013(SAND2013-2569): 53.
50. Chen J, Wang Q, Shen WZ, Pang X, Li S, Guo X. Structural optimization study of composite wind turbine blade. *Materials and Design* 2013; **46**: 247–255.
51. Peeters M, Santo G, Degroote J, Van Paepegem W. High-fidelity finite element

models of composite wind turbine blades with shell and solid elements. *Composite Structures* 2018; **200**: 521–531.
52. Holland JH (John H. *Adaptation in natural and artificial systems : an introductory analysis with applications to biology, control, and artificial intelligence*. Michigan: University of Michigan Press; 1975.
53. Goldberg DE. *Genetic algorithms in search, optimization, and machine learning*. California: Addison-Wesley; 1989.
54. Sastry K, Goldberg D, Kendall G. Genetic Algorithms. In: Burke E.K., Kendall G. (eds). *Search Methodologies*, Boston, MA: Springer US; 2005.
55. Wang L, Kolios A, Nishino T, Delafin PL, Bird T. Structural optimisation of vertical-axis wind turbine composite blades based on finite element analysis and genetic algorithm. *Composite Structures* 2016; **153**: 123–138.
56. Gentils T, Wang L, Kolios A. Integrated structural optimisation of offshore wind turbine support structures based on finite element analysis and genetic algorithm. *Applied Energy* 2017; **199**: 187–204.
57. Mazzoni S, Mckenna F, Scott MH, Fenves GL, Iii A. *Open System for Earthquake Engineering Simulation (OpenSees) OpenSees Command Language Manual*. 2006.
58. Foulser-Piggott R, Goda K. Ground-motion prediction models for arias intensity and cumulative absolute velocity for Japanese earthquakes considering single- station sigma and within-event spatial correlation. *Bulletin of the Seismological Society of America* 2015.
59. Chang Z, Sun X, Zhai C, Zhao JX, Xie L. An improved energy-based approach for selecting pulse-like ground motions. *Earthquake Engineering & Structural Dynamics* 2016; **45**(14): 2405–2411.
60. Chang Z, De Luca F, Goda K. Automated classification of near-fault acceleration pulses using wavelet packets. *Computer-Aided Civil and Infrastructure Engineering* 2019.
61. Miano A, Jalayer F, Ebrahimian H, Prota A. Cloud to IDA: Efficient fragility assessment with limited scaling. *Earthquake Engineering and Structural Dynamics* 2018; **47**(5): 1124–1147.
62. Jalayer F, Risi R De, Manfredi G. Bayesian Cloud Analysis : efficient structural fragility 2015: 1183–1203.
63. Wilkie D, Galasso C. A probabilistic framework for offshore wind turbine loss assessment. *Renewable Energy* 2020; **147**: 1772–1783.
64. DNV GL. *Design of Offshore Wind Turbine Structures (DNV-OS-J101)*. 2014.
65. Arany L, Bhattacharya S, MacDonald JHG, Hogan SJ. A critical review of serviceability limit state requirements for monopile foundations of offshore wind turbines. *Proceedings of the Annual Offshore Technology Conference*, vol. 4, Offshore Technology Conference; 2015.
66. EN 1993-1-6. Eurocode 3: Design of Steel Structures-Part 1-6: Strength and Stability of Shell Structures 2007.

Appendix

Table A.1. Pulse-like crustal records

Record #	Record ID	Event ID	*M*	*R* (km)	*Vs*30 (m/s)	Average *PGV* (cm/s)	Pulse / Characteristic period (T_p)			Pulse indicator (IsP)		
							X	Y	Z	X	Y	Z
1	126	41	6.80	5.46	659.60	65.03	4.2	0.6	0.7	1	0	0
2 [1 to 5]	143	46	7.35	2.05	766.77	108.39	2.2	5.3	2.8	1	1	0
3	170	50	6.53	7.31	192.05	49.02	1.4	3.5	1.4	0	1	0
4	171	50	6.53	0.07	186.21	70.28	2.5	2.8	2.2	1	1	1
5	173	50	6.53	6.17	202.85	46.42	3.2	1.7	6.1	1	1	0
6	179	50	6.53	7.05	208.91	69.89	2.0	4.4	2.1	0	1	0
7	180	50	6.53	3.95	205.63	72.15	2.6	3.9	2.0	1	1	1
8 [1 to 4]	181	50	6.53	1.35	203.22	83.89	2.6	3.5	0.1	1	1	0
9	182	50	6.53	0.56	210.51	78.29	3.1	3.4	2.0	1	1	1
10	183	50	6.53	3.86	206.08	52.90	1.6	4.1	4.5	0	1	1
11	184	50	6.53	5.09	202.26	56.21	3.2	1.0	4.6	1	0	1
12	185	50	6.53	7.65	202.89	47.47	4.4	3.5	4.2	1	1	0
13	802	118	6.93	8.50	370.79	46.13	1.6	5.4	1.5	1	1	1
14	825	123	7.01	6.96	513.70	84.38	0.2	2.1	4.5	0	1	1
15	828	123	7.01	8.18	712.82	69.59	0.8	0.7	5.3	0	1	1
16	879	125	7.28	2.19	684.94	97.16	4.1	3.3	1.6	1	1	1
17	983	127	6.69	5.43	525.79	74.57	3.2	1.5	2.1	1	0	1
18	1004	127	6.69	8.44	380.06	72.55	0.8	3.1	0.8	1	0	0
19	1045	127	6.69	5.48	285.93	78.15	2.1	1.8	0.9	1	1	1
20	1063	127	6.69	6.50	282.25	109.32	1.1	2.4	0.2	1	1	0
21	1086	127	6.69	5.30	440.54	94.35	1.8	1.8	0.9	1	1	0
22	1158	136	7.51	15.37	276.00	54.08	4.6	1.5	3.2	1	0	1
23	1193	137	7.62	9.64	427.73	51.37	3.9	5.6	4.4	1	1	0
24	1197	137	7.62	3.14	542.61	73.64	2.2	2.3	3.4	1	0	1
25	1231	137	7.62	2.69	553.40	103.46	1.0	1.1	1.0	0	1	0
26 [1 to 5]	1244	137	7.62	9.96	258.89	90.70	3.4	5.0	5.9	1	1	0
27	1476	137	7.62	28.05	473.90	48.47	7.8	4.9	6.0	1	1	1
28	1480	137	7.62	19.84	272.60	54.03	5.9	5.8	4.5	1	1	0
29	1481	137	7.62	25.44	272.60	45.45	8.3	6.6	5.0	1	1	1
30	1482	137	7.62	19.90	540.66	55.53	8.3	5.4	4.9	1	1	1
31	1489	137	7.62	3.78	487.27	53.87	9.8	5.1	6.3	1	1	1
32	1498	137	7.62	17.13	272.60	58.12	6.6	6.7	4.0	1	0	0
33	1501	137	7.62	9.80	272.60	66.24	6.2	4.2	4.2	0	1	1
34	1502	137	7.62	16.62	272.60	47.76	4.6	7.6	6.3	0	1	0
35 [1 to 5]	1503	137	7.62	0.59	305.85	101.64	4.8	2.3	4.2	1	0	1
36	1515	137	7.62	5.18	472.81	52.69	8.2	7.7	5.5	1	0	0
37	1528	137	7.62	2.13	272.60	57.12	6.0	5.6	4.5	1	1	1
38	1535	137	7.62	13.08	473.90	51.59	6.5	4.0	6.7	1	0	0
39	1542	137	7.62	25.44	215.00	58.49	5.8	4.9	7.2	1	0	0
40	1548	137	7.62	13.15	599.64	66.12	8.1	4.3	3.8	1	1	1

41	1549	137	7.62	1.84	664.43	47.32	1.1	6.1	0.9	0	1	0
42	1550	137	7.62	8.29	473.9	48.42	4.4	8.4	5	1	1	1
43 [3, 4]	1595	137	7.62	9.96	258.89	71.77	3.5	5.2	2.7	1	1	0
44	1602	138	7.14	12.04	326	59.17	5.4	1	0.1	0	1	0
45	1605	138	7.14	6.58	276	69.57	5	5.1	7.4	1	1	1
46	2114	169	7.90	2.74	329.4	98.51	2.3	4.9	3.7	1	1	1
47 [1 to 5]	37326	792	6.65	25.75	310.2	103.76	0.8	0.9	0.8	1	0	0
48	140627	1937	6.28	6.83	333.6	58.09	0.6	1.1	1.7	1	0	0
49	232727	2910	6.62	11.82	226.9	95.86	2.6	2.1	2.2	1	1	0
50	260367	3196	6.87	8.74	371.1	49.86	3.3	0.4	0.1	1	0	0

[1] Records leading to Y_{ULS} for C1.

[2] Records leading to Y_{ULS} for C2.

[3] Records leading to Y_{ULS} for C3.

[4] Records leading to Y_{ULS} for C4.

[5] Records leading to Y_{ULS} for C5.

IsP = 1; refers pulse-like ground motion component.

IsP = 0; refers non-pulse- like ground motion component.

Table A.2. Non-pulse-like crustal records

Record #	Record ID	Event ID	*M*	*R* (km)	*Vs*30 (m/s)	Average *PGV* (cm/s)	Pulse / Characteristic period (T_p)			Pulse indicator (IsP)		
							X	Y	Z	X	Y	Z
1	160	50	6.53	2.68	223.03	49.83	2.3	0.8	0.9	0	0	0
2	174	50	6.53	12.45	196.25	36.72	3.6	0.5	3.9	0	0	1
3	495	97	6.76	9.60	659.60	44.10	0.2	0.9	0.7	0	0	0
4	721	116	6.54	18.20	192.05	42.81	1.6	2.2	4.3	0	0	0
5	753	118	6.93	3.85	462.24	47.94	0.6	0.7	0.9	0	0	0
6	768	118	6.93	14.34	221.78	35.80	0.5	1.4	1.8	0	0	0
7	776	118	6.93	27.93	370.79	45.28	1.1	5.3	3.1	0	0	0
8	778	118	6.93	24.82	215.54	39.90	2.1	1.0	3.1	0	0	0
9	806	118	6.93	24.23	267.71	35.78	3.3	3.2	2.9	0	0	0
10	864	125	7.28	11.03	379.32	34.71	1.4	1.0	1.3	0	0	0
11	949	127	6.69	8.66	297.71	30.53	0.9	0.7	2.7	0	0	0
12	959	127	6.69	14.70	267.49	47.13	0.7	2.0	2.4	0	0	0
13	963	127	6.69	20.72	450.28	49.31	1.0	0.7	6.1	0	0	1
14	1044	127	6.69	5.92	269.14	83.75	1.6	1.4	0.2	0	0	0
15	1052	127	6.69	7.26	508.08	42.33	1.0	0.7	2.1	0	0	0
16	1077	127	6.69	26.45	336.20	32.06	2.0	2.7	2.2	0	0	0
17 [1 to 4]	1087	127	6.69	15.60	257.21	90.20	0.4	0.5	0.3	0	0	0
18	1111	129	6.90	7.08	609.00	36.05	0.7	0.8	0.5	0	0	0
19	1116	129	6.90	19.15	256.00	33.87	0.9	1.8	1.8	0	0	0
20	1141	134	6.40	3.36	219.75	32.76	2.7	2.1	1.6	0	0	0
21	1180	137	7.62	24.98	235.13	49.37	7.2	6.9	6.4	0	0	0
22	1203	137	7.62	16.06	233.14	38.37	4.0	6.9	2.6	0	0	0
23	1246	137	7.62	18.04	223.24	54.19	6.0	4.8	4.1	0	0	0
24	1495	137	7.62	6.36	272.60	37.03	2.5	8.0	5.5	0	0	1

25	1507	137	7.62	5.31	624.85	56.79	0.3	8.3	5.6	0	0	1
26	1508	137	7.62	7.03	468.14	60.33	0.9	0.7	8.2	0	0	1
27	1509	137	7.62	13.46	549.43	54.14	1.5	1.2	3.1	0	0	0
28	1512	137	7.62	8.20	443.04	34.93	0.9	0.5	6.2	0	0	0
29	1513	137	7.62	10.97	363.99	50.34	0.7	1.0	0.3	0	0	0
30	1517	137	7.62	11.24	553.40	90.31	1.9	2.7	0.8	0	0	0
31	1521	137	7.62	8.88	553.40	30.95	4.7	4.1	4.5	0	0	0
32	1532	137	7.62	17.18	473.90	38.74	5.9	9.0	5.4	0	0	0
33	1534	137	7.62	16.01	473.90	41.47	7.0	1.7	6.5	0	0	0
34	1536	137	7.62	11.60	212.72	57.91	2.5	2.0	4.6	0	0	0
35	1545	137	7.62	7.41	459.34	47.87	2.2	5.7	4.3	0	0	0
36	1547	137	7.62	14.93	272.60	40.25	7.0	3.8	4.7	0	0	0
37	1596	137	7.62	1.84	664.43	52.37	1.1	5.6	4.4	0	0	0
38	1633	144	7.37	12.56	723.95	47.29	2.8	2.5	1.8	0	0	1
39	1787	158	7.13	11.66	684.94	34.11	0.1	1.5	3.3	0	0	0
40	37157	792	6.65	15.07	167.70	43.87	1.5	1.4	1.6	0	0	0
41	37158	792	6.65	27.30	510.5	31.61	0.3	0.3	4.7	0	0	1
42	136605	1927	6.56	10.67	302.6	33.27	1.3	3.8	1.4	0	0	0
43 [1 to 5]	136607	1927	6.56	7.90	333.6	110.43	0.8	0.9	4.7	0	0	0
44	136608	1927	6.56	9.91	359.8	28.70	1	0.2	0.3	0	0	0
45	136609	1927	6.56	15.43	433.7	52.02	0.3	0.4	1.9	0	0	0
46	260166	3196	6.87	16.08	389.3	47.95	3.1	1.8	4.1	0	0	0
47	260167	3196	6.87	34.63	175.2	37.80	4.1	5.1	2.7	0	0	0
48	260365	3196	6.87	18.01	486.4	31.92	3.3	3.5	2.2	0	0	0
49	260366	3196	6.87	2.42	506.4	66.65	1.4	1.2	0.1	0	0	0
50	393116	4359	6.65	12.35	292.4	40.11	0.8	0.7	1	0	0	0

[1] Records leading to Y_{ULS} for C1.

[2] Records leading to Y_{ULS} for C2.

[3] Records leading to Y_{ULS} for C3.

[4] Records leading to Y_{ULS} for C4.

[5] Records leading to Y_{ULS} for C5.

IsP = 1; refers pulse-like ground motion component.

IsP = 0; refers non-pulse- like ground motion component.